

# Accurate simulation of pulled and pushed fronts in the nonautonomous Fisher-KPP equation

Troy Tsubota<sup>1,2,\*</sup>, Smridhi Mahajan<sup>1</sup>, Adrian van Kan<sup>1,3</sup>, and Edgar Knobloch<sup>1</sup>

<sup>1</sup>*Department of Physics, University of California at Berkeley, Berkeley, California 94720, USA*

<sup>2</sup>*Department of Physics, Harvard University, Cambridge, Massachusetts 02138, USA and*

<sup>3</sup>*Department of Mathematics, Texas A&M University, College Station, Texas 77843, USA*

(Dated: February 10, 2026)

We introduce a novel numerical method for direct simulation of front propagation in the Fisher-KPP equation with a time-dependent parameter on an infinite domain. The method computes a time-dependent boundary condition that accurately captures the leading-edge dynamics by coupling the nonlinear simulation region to a linear approximation region in which the dynamics can be solved exactly via the Green's function of the linearized equation. This approach enables precise front velocity measurements on relatively small computational domains for a variety of nonautonomous regimes and initial conditions for which existing numerical methods break down. We apply the method to pulled and pushed fronts in the Fisher-KPP equation with quadratic and quadratic-cubic nonlinearities, finding that, in all cases, it significantly improves the accuracy of the simulated front velocity even for constant parameters and a fixed domain size. For pulled fronts with a diffusion coefficient that increases algebraically in time, our results reveal a deviation from the natural asymptotic velocity predicted by linear theory, whose explanation requires nonlinear theory. For pushed fronts with constant parameters, the method reproduces the exponential convergence to the theoretical asymptotic front speed and profile with improved precision. For a slowly time-varying linear growth parameter, we find that the pushed front velocity follows the changing parameter adiabatically if the asymptotic pushed velocity remains faster than the natural asymptotic pulled velocity. As the growth parameter moves toward the pushed-pulled transition point, the competition between the pushed and pulled fronts can result in both delayed and even premature onset of the pushed-pulled transition, depending on the form of parameter growth. The numerical method presented here proves to be an effective tool enabling useful new insights into front propagation in nonautonomous systems by reducing finite domain effects and improving accuracy.

## I. INTRODUCTION

In this article, we analyze the one-dimensional Fisher-Kolmogorov-Petrovsky-Piskunov (F-KPP) equation [1, 2] with time-dependent parameters:

$$u_t = d(t)u_{xx} + f(u, t), \quad (1)$$

where  $f(0, t) = 0$ ,  $f(1, t) = 0$ ,  $f_u(0, t) > 0$ ,  $f_u(1, t) < 0$  and the subscripts denote partial derivatives. Thus,  $u = 0$  is a linearly unstable state, and the linearly stable state  $u = 1$  propagates into it. Following [3], we relax the classical KPP condition that  $f_u(u, t) < f_u(0, t)$  for  $u \in (0, 1)$ , which is imposed in the usual definition of a KPP-type equation [2, 4].

The F-KPP equation is the prototypical example of an equation that exhibits front propagation into an unstable state. Such front propagation, in which one pattern state invades another, is a ubiquitous phenomenon that arises in many physical and biological environments; see [3] for an extensive review of applications. In general, there are two types of

fronts. *Pulled* fronts are governed by linear dynamics at their leading edge [3], although in some cases, their properties are not determined by the leading edge alone [5]. *Pushed* fronts are governed by nonlinear dynamics in the bulk of the front [3]. Depending on the type and strength of the nonlinearities present, the F-KPP equation can exhibit both pulled and pushed fronts. Of great interest is the *front selection* problem [6] for which we seek to determine the selected front velocity and profile given an initial condition, e.g., a localized perturbation.

Front selection in the autonomous F-KPP equation has been rigorously studied [7–9]. Subsequent works established the *marginal stability criterion* [3, 6, 10] for pulled fronts, which states that for sufficiently steep initial conditions, the front approaches the marginally stable front solution with asymptotic velocity and steepness determined by linear dynamics. This criterion has been shown to hold for a wide class of equations [3, 10, 11] among other related ideas such as marginal positivity [3, 6]. Pushed fronts have also been well-studied in the autonomous case, giving rise to the concept of *nonlinear marginal stability*, although analyses are specific to the choice of nonlinearity [3, 12, 13].

On the other hand, front selection in the nonautonomous case is not as well established, and its

\* [troytsubota@g.harvard.edu](mailto:troytsubota@g.harvard.edu)

understanding would provide insight into important problems such as pattern formation on growing domains [14–16], relevant to the growth of organisms, and ecological systems within a time-varying environment [17, 18]. Previous studies [4, 16, 19–21] have made some progress on the nonautonomous front selection problem, particularly for the F-KPP equation. Pulled fronts in the nonautonomous F-KPP equation admit a *natural asymptotic velocity* and *natural asymptotic steepness*, which differ from the velocity and steepness expected from the marginal stability criterion [16]. However, these studies are restricted to limited parameter regimes. Furthermore, while the natural asymptotic velocity and steepness have been shown to be useful quantities, there are currently no general guarantees that the front asymptotically converges to this velocity and steepness. Nonautonomous pushed fronts also remain largely unexplored.

To make progress towards a more general theory, we turn to numerical simulations. Direct numerical simulation of the F-KPP equation is challenging—one often avoids direct simulations and instead uses numerical continuation to seek steady front solutions in a comoving frame [6]. However, this is not possible nor desired for the nonautonomous problem. One key challenge with direct numerical simulation is that we are interested in the dynamics on an infinite domain, yet we can only simulate finite ones. If insufficient care is taken in the formulation on the finite domain, the properties of the solution may be qualitatively altered, not unlike the effect of a small-amplitude cut-off, which is known to shift front speeds, among other effects [22, 23]. The challenge posed by the finiteness of the domain is typically addressed by making the domain large and enforcing what one may consider reasonable boundary conditions, e.g., zero Dirichlet or zero Neumann. However, for pulled fronts, the behavior at the leading edge ( $x \rightarrow \infty$ ) is critical [3, 24], so naïve boundary conditions do not capture the dynamics accurately.

To examine this more closely, refer to Fig. 1. The leading edge of a front in the F-KPP equation generally has an exponential tail  $u(x, t) \sim e^{-\lambda x}$  as  $x \rightarrow \infty$ , where  $\lambda$  is the steepness (Fig. 1(a)). Roughly speaking, for a pulled front, the steepness dictates its speed: if the front is steeper, it moves more slowly. A good boundary condition would faithfully represent this exponential tail. However, neither a zero Dirichlet condition  $u(x_1) = 0$  nor a zero Neumann condition  $u_x(x_1) = 0$  can satisfy this requirement. For a zero Dirichlet condition (Fig. 1(b)), pinning the front at zero prevents it from developing into its desired exponential tail structure. The front propagates at a systematically reduced speed [24, 25],

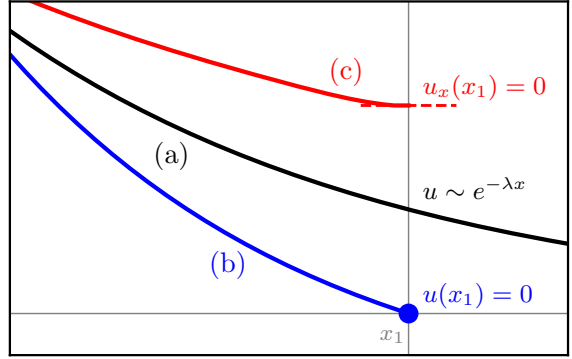


FIG. 1. Naïve choices for the boundary condition do not accurately capture the dynamics at the leading edge of a front in the F-KPP equation. (a) The exponential leading edge of a front with steepness  $\lambda$ . A desirable “infinity-simulating” boundary condition would give correct values for  $u(x_1)$  and  $u_x(x_1)$  of this tail, where  $x_1$  is the boundary of the direct numerical simulation. (b) A zero Dirichlet boundary condition  $u(x_1) = 0$  results in a front that is too steep and therefore too slow. (c) A zero Neumann boundary condition  $u_x(x_1) = 0$  results in a front that is too shallow and therefore too fast.

which can be particularly extreme for shallow fronts. Conversely, a zero Neumann boundary condition (Fig. 1(c)) forces the leading edge to be shallower than it should be, resulting in a faster propagating front. In fact, the Neumann condition creates a flat state in long times that will grow uniformly [24].

Several approaches have been proposed to resolve this issue. One useful approach is to work in a comoving frame, which allows the front to remain away from the simulation boundaries for longer times. While it is useful for keeping a small computational domain size, a moving frame alone does not significantly improve the simulation accuracy in long times because the effect of the naïve boundary condition will propagate into the interior of the computational domain [24]. A Robin boundary condition may seem to provide a proper mix of the Dirichlet and Neumann conditions. In fact, for steepness  $\lambda$ , the Robin condition  $u_x + \lambda u = 0$  would represent this exponential tail precisely. However, this technique only works for shallow initial conditions. Steep initial conditions approach the asymptotic steepness from above, so enforcing this Robin condition starting at  $t = 0$  would impose an incorrect constraint at early times. This technique also requires a priori knowledge of the front steepness that we do not have in the nonautonomous case. Another related approach accounts for the exponential tail by setting a nonzero Dirichlet boundary condition with an exponential form [26], yet similar problems arise.

This problem of simulating an infinite domain on a finite computational domain has been studied for other equations [27, 28]; it is related to the problem of non-reflecting boundary conditions, also known as perfectly matched layers, in wave propagation [29, 30]. In particular, for equations that reduce to the heat equation in the far-field, [31] introduces a Green's function approach to construct exact boundary conditions. The method analytically eliminates the exterior infinite domain and replaces it with a Neumann-to-Dirichlet relation that prescribes the correct boundary value by integrating over the flux into the exterior region. The study also introduces the notion of a buffer region between the interior and exterior region so that the resulting convolutions with the Green's function are well-behaved and can be reliably computed numerically. An earlier version of this approach was applied to the Fisher equation in [32] using a Laplace transform on the linearized equation outside of the domain. However, arbitrary time-dependent parameters are difficult to incorporate into the Laplace transform formulation.

Here, we combine the insights from previous work and apply them to the nonautonomous problem. We shift into a moving frame and introduce an infinity-simulating boundary condition built on the exact Green's function associated with the linearized F-KPP equation that accurately represents the leading-edge dynamics. We refer to this method as the Green's (function) boundary condition (GBC) method in the following. This approach removes spurious boundary effects and allows reliable long-time front dynamics to be computed accurately on much smaller domains. We demonstrate this below for a variety of time-dependent regimes in both pulled and pushed settings. We focus on two key cases: the nonautonomous F-KPP with a quadratic nonlinearity, i.e. the Fisher equation, and the nonautonomous F-KPP with a quadratic-cubic nonlinearity.

## II. NUMERICAL APPROACH

In the general case, we seek to simulate Eq. (1) on an infinite domain  $x \in (-\infty, \infty)$ . We shift into a moving frame with a prescribed velocity  $c(t)$  (not necessarily comoving with the front) to obtain

$$u_t = d(t)u_{xx} + c(t)u_x + f(u, t). \quad (2)$$

The key idea behind the GBC method is that *the leading edge is governed by linear dynamics*. We can select  $c(t)$  to be fast enough so that the leading edge values remain small for the entire simulation time. For instance, the comoving velocity would satisfy this requirement.

Now, refer to Fig. 2 for the high-level approach. The domain can be decomposed into two regions: the nonlinear simulation (NL) region on  $[x_0, x_1]$  and the linear approximation (LA) region on  $[x_1 - \delta, \infty)$  with  $\delta > 0$ . The NL and LA regions communicate through their boundaries. More precisely, suppose we begin with a compact initial condition  $u(x, 0)$  on  $[x_0, x_1 - \delta]$ , so that  $u$  is initially identically zero in the LA region. Then, the NL region value  $g(t) = u(x_1 - \delta, t)$  is a boundary forcing for the LA region and completely determines the solution in the LA region. This can be formulated as the problem

$$u_t = a(t)u + c(t)u_x + d(t)u_{xx}, \quad (3)$$

$$u(x, 0) = 0, \quad x > x_1 - \delta, \quad (4)$$

$$u(x_1 - \delta, t) = g(t), \quad t > 0, \quad (5)$$

to be solved in the LA region  $x \in [x_1 - \delta, \infty)$ . The function  $a(t)$  comes from the linearization of  $f(u, t)$  around  $u = 0$ . Given a boundary Green's function  $G_b(x, t; y, s)$  for this equation (for the heat equation, see [33]), we can write the solution in the LA region as

$$u(x, t) = \int_0^t G_b(x, t; x_1 - \delta, s)g(s)ds. \quad (6)$$

In particular, we can compute  $u(x_1, t)$ . Conversely, we can use the value  $u(x_1, t)$  as a time-dependent Dirichlet boundary condition for the NL region.

The detailed computation of the Green's function is rather involved; see Appendix A for the complete treatment. Importantly, we are able to obtain closed-form expressions for the Green's function and its convolution integrals under the key assumption that  $c(t) = \gamma d(t)$  for some constant  $\gamma$ . This assumption is not too restrictive since we can tune  $\gamma$  as desired, but it is important to recognize that we cannot necessarily move at a comoving velocity. Additionally, the Green's function formulation allows for a straightforward generalization to nonzero initial conditions in the LA region.

The GBC method proceeds as follows (Fig. 2). We discretize time with a time step  $dt$ . At each time step, we perform the following two steps:

1. Use the NL region value  $g(t) = u(x_1 - \delta, t)$  to compute  $u(x_1, t + dt)$  in the LA region by convolving with the boundary Green's function.
2. Use  $u(x_1, t + dt)$  as a Dirichlet boundary condition to compute  $u(x, t + dt)$  from  $u(x, t)$  in the NL region by a numerical time step.

For our simulations, we specifically use second-order central finite differences in space and an implicit-explicit (IMEX) Euler scheme in time, which treats the linear terms  $a(t)u + c(t)u_x + d(t)u_{xx}$

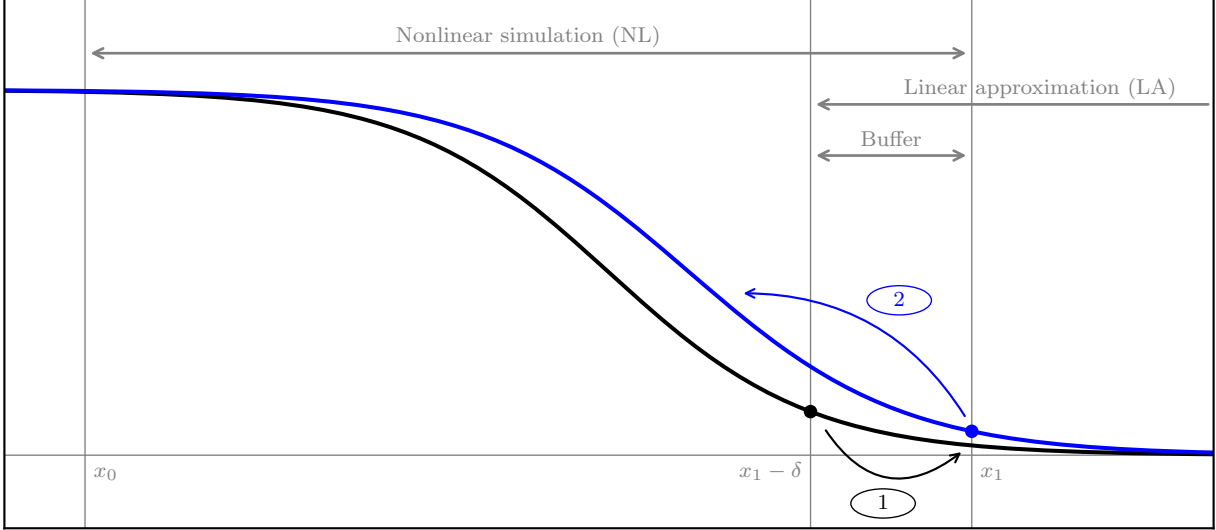


FIG. 2. In the Green's (function) boundary condition (GBC) method, the domain is split into two regions: the nonlinear (NL) simulation region and the linear approximation (LA) region. These regions overlap in a buffer region of size  $\delta$  required for regularization. At each time step, (1) the value  $u(x_1 - \delta, t)$  acts as a boundary forcing for the LA region to predict  $u(x_1, t + dt)$ . Then, (2) the updated value  $u(x_1, t + dt)$  is the new boundary condition for an implicit step to compute  $u(x, t + dt)$  within the NL region. The left boundary condition is a zero-flux condition  $u_x(x_0, t) = 0$ .

implicitly and nonlinear terms in  $f(u, t)$  explicitly. We implement a simple Neumann boundary condition  $u_x(x_0, t) = 0$  at the left boundary; since the system saturates at the stable state  $u = 1$  there, this boundary does not significantly affect the front dynamics in the F-KPP equation. However, one could implement a similar linear approximation for the left boundary by linearizing about the stable  $u = 1$  state in the region  $(-\infty, x_0]$ .

Compared to a typical finite-difference solver, several new numerical considerations must be taken into account, such as the evaluation of the convolution integrals, the size of the buffer region, and the speed of the frame. These details, which are not important for understanding the main results, are discussed in Appendix B.

### III. PULLED FRONTS

#### A. Autonomous pulled fronts

To benchmark the GBC method, we first consider the simpler autonomous Fisher equation

$$u_t = u_{xx} + u - u^2. \quad (7)$$

It is well-known that for steep initial conditions, e.g. a step function, delta function, or Gaussian, the asymptotic velocity of a front in Eq. (7) is  $v^* = 2$

via the marginal stability criterion or other methods. Furthermore, the asymptotic approach to this velocity is [3, 9, 10]

$$\Delta v(t) = v(t) - v^* = -\frac{3}{2t} + \text{h.o.t.} \quad (8)$$

This  $\mathcal{O}(1/t)$  scaling can also be recovered from a simple linear argument as follows. The exact solution to Eq. (7) linearized about  $u = 0$  with a delta function initial condition is

$$u(x, t) = \frac{1}{\sqrt{4\pi t}} \exp\left(t - \frac{x^2}{4t}\right). \quad (9)$$

Tracking the front at a height  $u = H$  gives the exact position

$$x_{H,\text{lin}}(t) = 2t \left[1 - \frac{1}{2t} \ln(Ht)\right]^{1/2}. \quad (10)$$

Expanding as  $t \rightarrow \infty$  gives a velocity deviation of

$$\Delta v_{\text{lin}}(t) = v_{H,\text{lin}}(t) - v^* = -\frac{1}{2t} + \text{h.o.t.} \quad (11)$$

While the  $1/t$  coefficient differs between the linear and nonlinear cases [3], the  $\mathcal{O}(1/t)$  scaling is the same.

We use the GBC method to simulate Eq. (7) with a step function initial condition  $u(x, 0) = 1$  for  $x \leq 0$  and  $u(x, 0) = 0$  for  $x > 0$ . For comparison, we

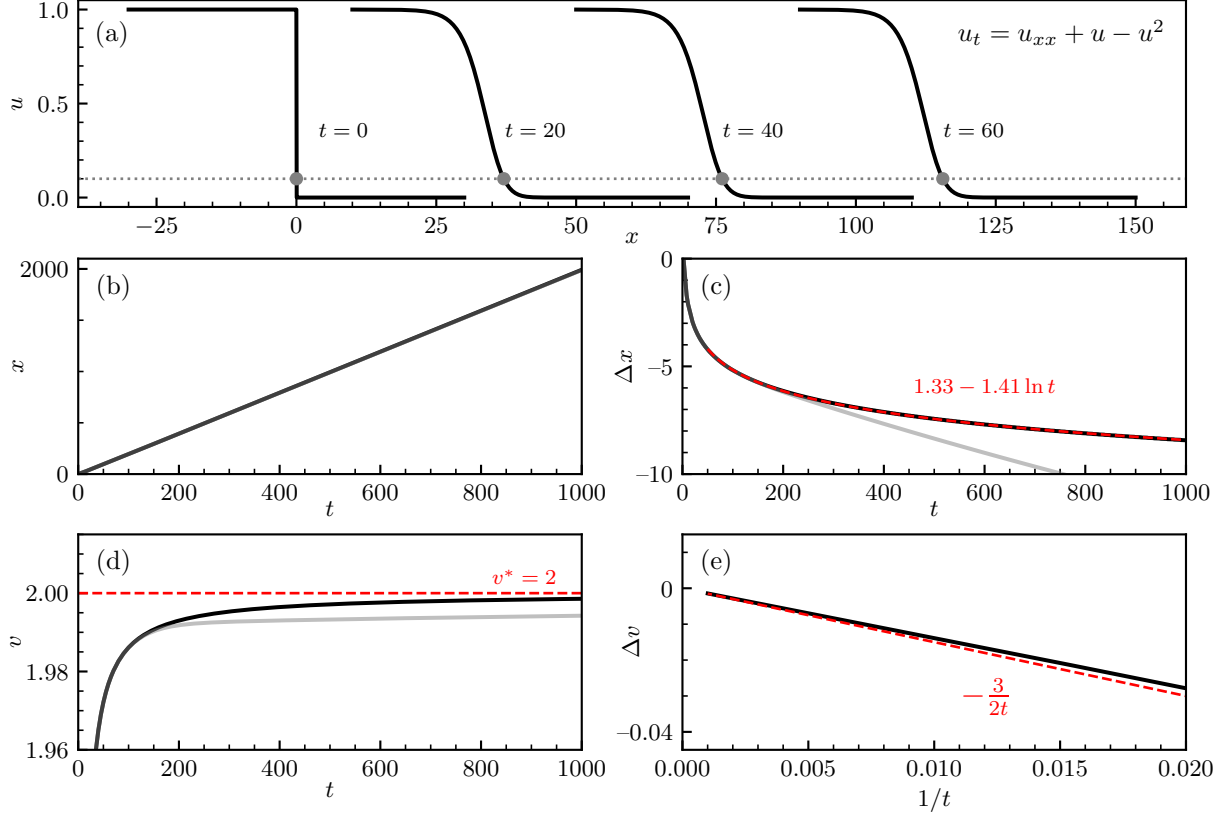


FIG. 3. The GBC method benchmarks well for the simplest case of the autonomous Fisher equation (7) with a step function initial condition. Simulations use  $dt = 0.025$ ,  $t \in [0, 1000]$ ,  $dx = 0.01$ ,  $x \in [-30, 30]$ , with a moving frame of speed  $c = v^* = 2$ . A buffer region of size  $\delta = 10$  is used for the GBC nonlinear-linear transition (see Fig. 2). (a) Lab-frame visualization of the propagating front. The solid, black curves at  $t = 0, t = 20, t = 40$ , and  $t = 60$  are the numerically simulated profiles obtained with the GBC method. The dotted, gray line with solid points indicates the tracked front position at  $u = 0.1$ . (b) Front position  $x(t)$  in the lab frame with the GBC method (solid, black) and a naïve zero Dirichlet condition (solid, gray). The difference in this plot is not perceptible. (c) Front position  $\Delta x(t) = x(t) - v^* t$  in the moving frame for the two cases. Here, we clearly see that the GBC front correctly follows the theoretical  $\ln t$  scaling (fitted with a red dashed line), while the DZ (Dirichlet zero) front does not. (d) Front velocity  $v(t)$  in the lab frame, computed by averaging over a time window  $\Delta t = 5 = 200 dt$ . The asymptotic value  $v^* = 2$  (dashed, red) is approached from below in the GBC method, but the velocity undershoots in the DZ method. This slowdown in the DZ case is expected (cf. Fig. 1). (e) Front velocity deviation from the asymptotic value  $\Delta v(t) = v(t) - v^*$  over  $1/t$  approaches the  $-3/2t$  line (dashed, red) as  $t \rightarrow \infty$ , in agreement with theory [3, 9, 10].

define the Dirichlet zero (DZ) method as the same method with the same parameters but without the dynamic boundary condition. We show the results in Fig. 3, which indicates that the GBC method performs well for a steep initial condition: the front correctly approaches  $v^* = 2$  from below with the predicted  $-3/2t$  scaling, while the DZ method results in an incorrect velocity that undershoots  $v^*$ . The DZ method forces the front to be too steep, as depicted in Fig. 1, resulting in a slower front.

As described in [3], the meaning of a “steep” initial condition is that the tail as  $x \rightarrow \infty$  falls off faster than  $e^{-\lambda^* x}$ , where  $\lambda^*$  is the asymptotic steepness. For Eq. (7), one finds  $\lambda^* = 1$ . An exponential

initial condition with steepness  $\lambda_0 < \lambda^*$  is considered a “shallow” (or “flat”) initial condition [24]. In this case, the front does not approach the marginally stable front solution but instead converges to a uniformly translating solution with the same steepness  $\lambda_0$  and speed  $v = \lambda_0 + 1/\lambda_0 > v^*$  [3]. For  $\lambda_0 = 2/\sqrt{6}$ , this front has a known exact solution (up to translation invariance) given by

$$u^*(x) = \left\{ 1 + \exp \left[ \sqrt{\frac{1}{6}} \left( x - \frac{5}{\sqrt{6}} t \right) \right] \right\}^{-2} \quad (12)$$

with speed  $v = 5/\sqrt{6}$  [26].

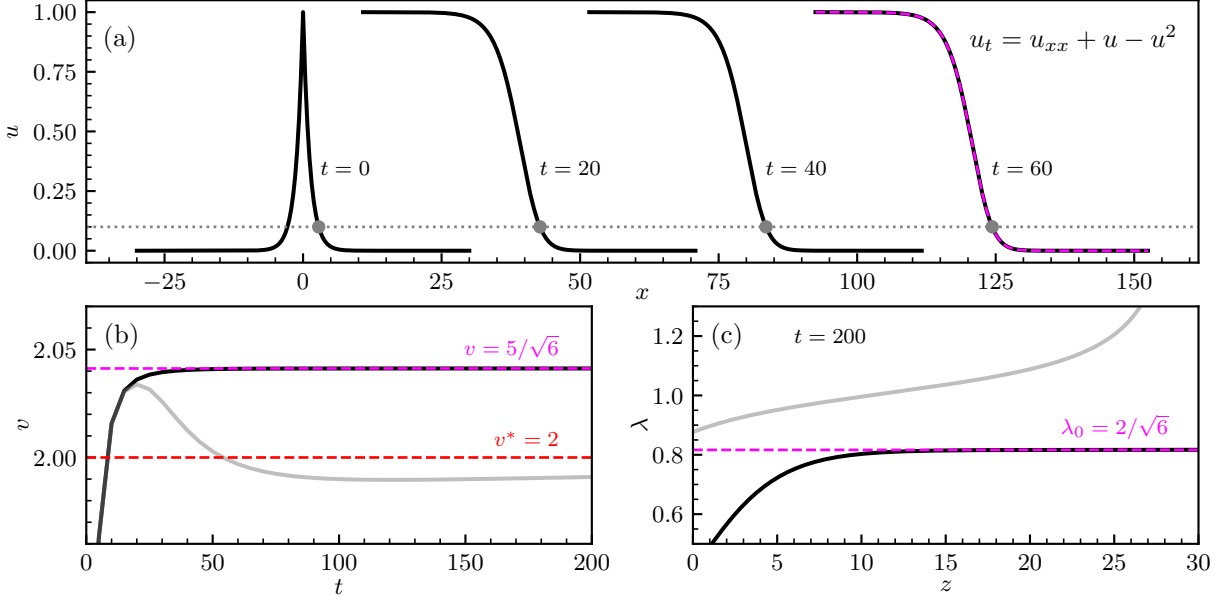


FIG. 4. The GBC method also benchmarks well for Eq. (7) with an exponential initial condition  $e^{-\lambda_0|x|}$ . Here,  $\lambda_0 = 2/\sqrt{6}$  which is less than the critical steepness  $\lambda^* = 1$ . We set the moving frame speed  $c$  to be the asymptotic speed  $v = \lambda_0 + 1/\lambda_0 = 5/\sqrt{6}$ . (a) Numerically simulated front (solid, black) with an exponential initial condition propagates through the lab frame. This particular case has the known exact asymptotic solution given in Eq. (12). At  $t = 60$ , the numerical solution shows good agreement with this exact solution (magenta, dashed). (b) Front velocity over time shows that the GBC front (solid, black) correctly attains the theoretical asymptotic velocity  $v = 5/\sqrt{6}$  (magenta, dashed), while the DZ front (solid, gray) eventually falls below  $v^* = 2$  (red, dashed). (c) Local steepness  $\lambda = -u_x/u$  in the moving frame coordinate  $z = x - \int_0^t c(t') dt'$  at  $t = 200$  shows that the GBC front steepness correctly approaches  $\lambda_0 = 2/\sqrt{6}$  at the leading edge while the DZ front does not.

The GBC method unlocks the ability to accurately study this front profile. Under the DZ method, the front steepness diverges and profile measurements become increasingly unreliable as the edge of the domain is approached. The GBC method resolves this issue by assigning the correct value of the front at the boundary, which allows for the front to be well behaved here, enabling study of the profile even in small domains.

In Fig. 4, we show that the GBC method also performs well for the shallow exponential initial condition  $u(x, 0) = e^{-\lambda_0|x|}$  with  $\lambda_0 = 2/\sqrt{6}$ . The GBC front correctly approaches  $v = 5/\sqrt{6}$ , and the profile agrees with the exact solution at long times. The DZ front eventually falls below  $v^* = 2$  because the naïve boundary condition does not faithfully represent the shallow leading edge, and the front regresses to the steep initial condition regime.

Already in the autonomous case, the power of the GBC method becomes apparent. The method can handle both the steep and shallow cases within the same framework. This contrasts with previous methods that require different boundary conditions for each case.

## B. Nonautonomous pulled fronts

We begin with the nonautonomous Fisher equation

$$u_t = a(t)u + d(t)u_{xx} - a(t)u^2 \quad (13)$$

and linearize about  $u = 0$ :

$$u_t = a(t)u + d(t)u_{xx}. \quad (14)$$

Using linear theory, one can deduce that the long-time behavior of pulled fronts in Eq. (13) may be described by the *natural asymptotic velocity* and *natural asymptotic steepness* [16], defined as

$$v^{**}(t) = \frac{A(t)d(t) + D(t)a(t)}{\sqrt{A(t)D(t)}}, \quad (15)$$

$$\lambda^{**}(t) = \sqrt{\frac{A(t)}{D(t)}}, \quad (16)$$

where  $A(t) = \int_0^t a(t') dt'$  and  $D(t) = \int_0^t d(t') dt'$ . These differ from the time-frozen asymptotic velocity  $v^*(t)$  and steepness  $\lambda^*(t)$ , indicating that the

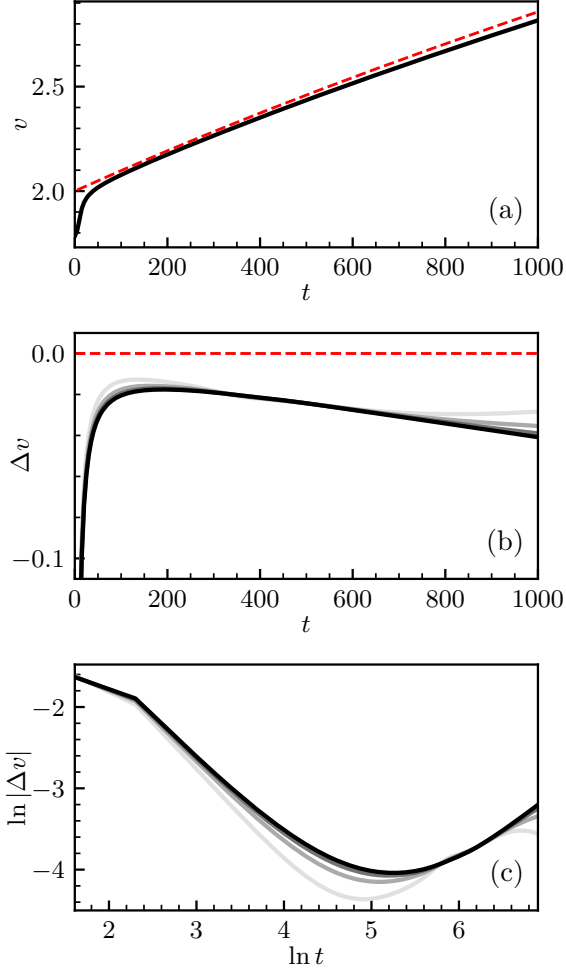


FIG. 5. The GBC method applied to the Fisher equation with linearly increasing time-dependent diffusion coefficient  $d(t) = 1 + \epsilon t$ ,  $\epsilon = 0.001$ . The numerical simulation parameters are  $dt = 0.025$ ,  $t \in [0, 1000]$ ,  $dx = 0.01$ ,  $x \in [-90, 90]$  with a moving frame  $c(t) = \gamma d(t)$  with  $\gamma = 1.65$  and a buffer region of size  $\delta = 10$ . (a) The numerical front velocity  $v(t)$  (solid, black) deviates from the natural asymptotic velocity  $v^{**}(t)$  (red, dashed) as  $t \rightarrow \infty$  in disagreement with linear theory. (b) The velocity difference  $\Delta v(t) = v(t) - v^{**}(t)$  reveals this disagreement more clearly. Simulations with  $dt \in \{0.2, 0.1, 0.05, 0.025\}$  are shown in progressively darker shades of gray, with the  $dt = 0.025$  simulation depicted in (a) drawn in black. (c) A log-log plot of  $\Delta v(t)$  suggests the existence of short- and long-time asymptotic algebraic regimes.

marginal stability criterion does not hold in the nonautonomous case. For more details, see [16].

However, there are no general guarantees that the front velocity converges to  $v^{**}(t)$  in the fully nonlinear setting, unless  $a(t)$  grows linearly [19] and in some cases of bounded parameters [4], and the au-

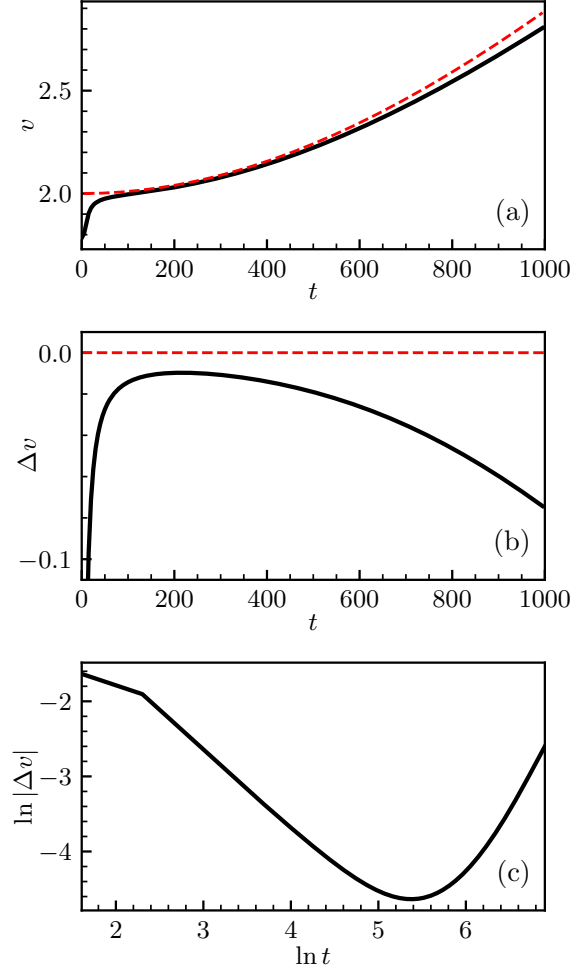


FIG. 6. As in Fig. 5, a quadratically increasing diffusion coefficient  $d(t) = 1 + (\epsilon t)^2$  with  $\epsilon = 0.001$  also indicates two-stage algebraic asymptotics.

thors are unaware of any general results on the convergence asymptotics in the nonlinear regime. In the autonomous case described above, the nonlinear leading-order asymptotics of the front velocity agree with the linear asymptotics up to a multiplicative constant. We follow the same procedure here to obtain a preliminary rate of convergence of the nonautonomous front to its natural asymptotic velocity.

The exact solution to Eq. (14) for a delta function initial condition is

$$u(x, t) = \frac{1}{\sqrt{4\pi D(t)}} \exp \left( A(t) - \frac{x^2}{4D(t)} \right). \quad (17)$$

Solving for the front position at a tracking height  $H$

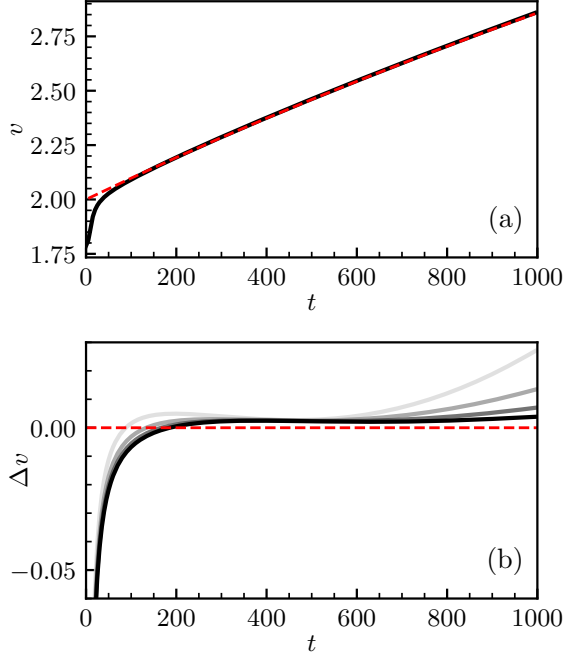


FIG. 7. In contrast to the linearly increasing diffusion coefficient (Fig. 5), a linearly increasing growth coefficient  $a(t) = 1 + \epsilon t$  with  $\epsilon = 0.001$  shows convergence as  $dt$  is reduced, in agreement with the rigorous proof [19].

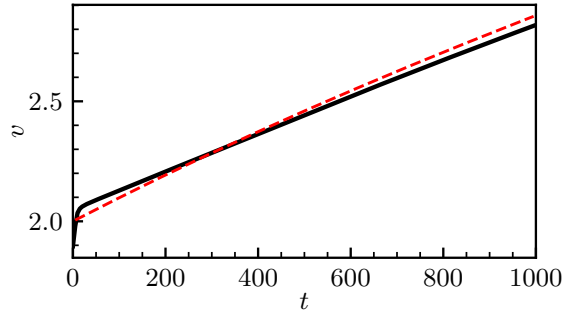


FIG. 8. The same linearly increasing diffusion coefficient  $d(t) = 1 + \epsilon t$  with  $\epsilon = 0.001$  as in Fig. 5 but with an exponential initial condition  $u(x,0) = e^{-\lambda|x|}$ ,  $\lambda = 0.9$ . Initially, the front steepness is less than the natural asymptotic steepness, i.e.  $\lambda < \lambda^{**}(0) = 1$ , so the front propagates faster than the natural asymptotic velocity. However, since  $\lambda^{**}(t)$  decreases and  $v^{**}(t)$  increases with increasing  $t$ , the front velocity eventually falls below the natural asymptotic velocity.

gives the exact front position

$$x_H(t) = 2\sqrt{A(t)D(t)} \left[ 1 - \frac{1}{2A(t)} \ln \left( \frac{D(t)^2}{H\sqrt{4\pi}} \right) \right]^{1/2}. \quad (18)$$

In order to proceed further, we restrict to asymptotically algebraic growth of  $a(t)$  and  $d(t)$  so that we can Taylor expand the second term in Eq. (18) in the limit  $t \rightarrow \infty$ . This results in

$$x_H(t) = x^{**}(t) - \frac{1}{2} \sqrt{\frac{D(t)}{A(t)}} \ln \left( \frac{D(t)^2}{H\sqrt{4\pi}} \right) + \text{h.o.t.}, \quad (19)$$

where  $x^{**}(t) = \int_0^t v^{**}(s) ds = 2\sqrt{A(t)D(t)}$  is the *natural asymptotic position* as described in [16].

Let  $a(t) = \mathcal{O}(t^\alpha)$  and  $d(t) = \mathcal{O}(t^\beta)$  as  $t \rightarrow \infty$  for some  $\alpha, \beta \geq 0$ . Thus  $A(t) = \mathcal{O}(t^{\alpha+1})$  and  $D(t) = \mathcal{O}(t^{\beta+1})$ . It follows that the deviation of the instantaneous front position from its natural asymptotic position scales as

$$\Delta x(t) = x_H(t) - x^{**}(t) = \mathcal{O}\{t^{(\beta-\alpha)/2} \ln t\}. \quad (20)$$

And if  $\beta - \alpha \neq 0$ , the front velocity deviation scales as

$$\Delta v(t) = v_H(t) - v^{**}(t) = \mathcal{O}\{t^{(\beta-\alpha)/2-1} \ln t\}. \quad (21)$$

For  $\beta - \alpha = 0$ , we have instead  $\Delta v(t) = \mathcal{O}(1/t)$  as in the autonomous case.

For example, for  $a(t) = 1$  and  $d(t) = 1 + \epsilon t$ , we expect  $\Delta v(t) \sim t^{-1/2} \ln t$  as  $t \rightarrow \infty$ . This suggests that the front velocity should converge to the natural asymptotic velocity  $v^{**}(t)$  as  $t \rightarrow \infty$ . In general, based on Eq. (21), we expect convergence to the natural asymptotic velocity if  $\beta - \alpha < 2$ .

We can now use the GBC method to simulate Eq. (13) and test these linear asymptotic predictions. For a linearly increasing diffusion coefficient  $d(t) = 1 + \epsilon t$  with  $\epsilon = 0.001$  and a constant growth coefficient  $a(t) = 1$ , the results are shown in Fig. 5. We see that, for a step function initial condition, the front velocity does not converge to the natural asymptotic velocity, contrary to the predictions of linear theory. In fact, when examining  $\ln |\Delta v|$  over  $\ln t$  as in Fig. 5(c), the asymptotic behavior is quite complex. Initially, the velocity deviation appears to decrease algebraically in a transient regime. However, at long times, the velocity deviation appears to increase algebraically. This is rather surprising and indicates that the nonlinear dynamics are more subtle than the linear predictions. This two-stage algebraic behavior is more pronounced for the quadratically increasing diffusion coefficient  $d(t) = 1 + (\epsilon t)^2$  as shown in Fig. 6, although in this case, linear theory does not predict convergence.

To confirm that this is not an artifact of the numerical method, we perform a range of simulations with  $dt \in \{0.2, 0.1, 0.05, 0.025\}$  as shown in Fig. 5(b). The deviation from the natural asymptotic velocity persists as  $dt$  is reduced, indicating

that this is indeed a physical effect rather than a discretization error. Additionally, in Fig. 7, we show that a linearly increasing growth coefficient  $a(t) = 1 + \epsilon t$  with constant diffusion ( $\alpha = 1$ ,  $\beta = 0$ ) converges to the natural asymptotic velocity as proven in [19]. Comparing Fig. 3(d) with Fig. 7(b) and relying on the intuition provided by linear theory (21), our results suggest that a monotonically increasing  $a(t)$  enables faster convergence to the natural asymptotic velocity than in the autonomous case.

Note that the shapes of the curves in Fig. 5 are also influenced to some extent by the manually selected speed of the frame. However, an appropriate choice of frame speed does not influence the overall result. See Appendix B for further commentary on the choice of the frame speed parameter  $\gamma$ .

Another effect we observe with the GBC method is that of a time-dependent parameter on a shallow initial condition. For example, for  $d(t) = 1 + \epsilon t$  and an exponential initial condition  $u(x, 0) = e^{-\lambda|x|}$  with  $\lambda = 0.9 < \lambda^{**}(0) = 1$ , Fig. 8 shows that, as expected, the front velocity initially exceeds the natural asymptotic velocity. However, as  $d(t)$  increases, the natural asymptotic steepness  $\lambda^{**}(t)$  decreases and the front velocity eventually falls below the natural asymptotic velocity. There is no analogous phenomenon in the autonomous case, and naïve boundary conditions would not be able to capture this effect reliably or accurately because the shallow initial condition cannot be faithfully represented.

## IV. PUSHED FRONTS

### A. Autonomous pushed fronts

To examine the pushed front regime, we consider the following modification to the F-KPP equation:

$$u_t = u_{xx} + au + u^2 - (1 + a)u^3. \quad (22)$$

This quadratic-cubic nonlinearity is the same as that in the Nagumo equation [35, 36], except that in this case, following [24], the parameter  $a$  is now located in the linear and cubic terms. For  $a > 1$ , pulled fronts are selected in Eq. (22). For  $a < 1$ , pushed fronts emerge with asymptotic front steepness and velocity

$$\lambda^\dagger = \sqrt{\frac{a+1}{2}}, \quad (23)$$

$$v^\dagger = 3\lambda^\dagger - \frac{1}{\lambda^\dagger}. \quad (24)$$

An analytical expression for the asymptotic front solution is also given in [24] (up to translation invari-

ance):

$$u^\dagger(x, t) = \frac{e^{-\lambda^\dagger(x - v^\dagger t)}}{1 + e^{-\lambda^\dagger(x - v^\dagger t)}}. \quad (25)$$

We simulate Eq. (22) using the GBC method and find that it is in agreement with the theoretical predictions as depicted in Fig. 9. The front profile approaches  $u^\dagger$ , as shown in Fig. 9(a). Since pushed front propagation is dictated by nonlinear bulk dynamics and the GBC method works exclusively on the leading edge, improved accuracy for pushed fronts is not necessarily expected. This is depicted in Fig. 9(b), where the velocity plots of the GBC and DZ methods nearly overlap. However, a closer look at the front velocity deviation in Fig. 9(c) reveals a major difference in the precision of front tracking between the two methods. The GBC method improves agreement with the analytical solution by several orders of magnitude, indicating the importance of the appropriate boundary condition across regimes.

While the velocity of pushed fronts is known to converge exponentially [12], there is no known method of derivation or a prediction of the convergence rate for Eq. (22). We therefore turn to results from numerical simulations to estimate the specific time constant. We perform a log-linear fit, where the fitting region is chosen according to [34], to obtain  $\tau_v \approx 36$ . Note that we are only able to perform fitting for early times after which the error  $\Delta v$  tapers off. This is indicative of a persistent numerical error due to finite resolution and gives us a way to separate the discretization error from the boundary method error. The GBC method allows for a larger fitting region for the expected exponential convergence, thus providing a more reliable estimate of the velocity convergence time constant.

As with the velocity convergence, the profile of pushed fronts also exhibits exponential convergence [12], and we naturally expect the two rates to be the same. We follow the same fitting procedure as for  $\tau_v$  to obtain the time constant for front steepness convergence,  $\tau_\lambda \approx 41$ . The profile measurements are more robust than the velocity measurements, since the latter rely on discrete time intervals in addition to discrete space; indeed, this higher degree of accuracy of the profile is consistent with the observed the longer scaling region in Fig. 9(e) compared to Fig. 9(c). We conclude that our numerically measured values for  $\tau_v$  and  $\tau_\lambda$  are reasonably close to one another, as expected.

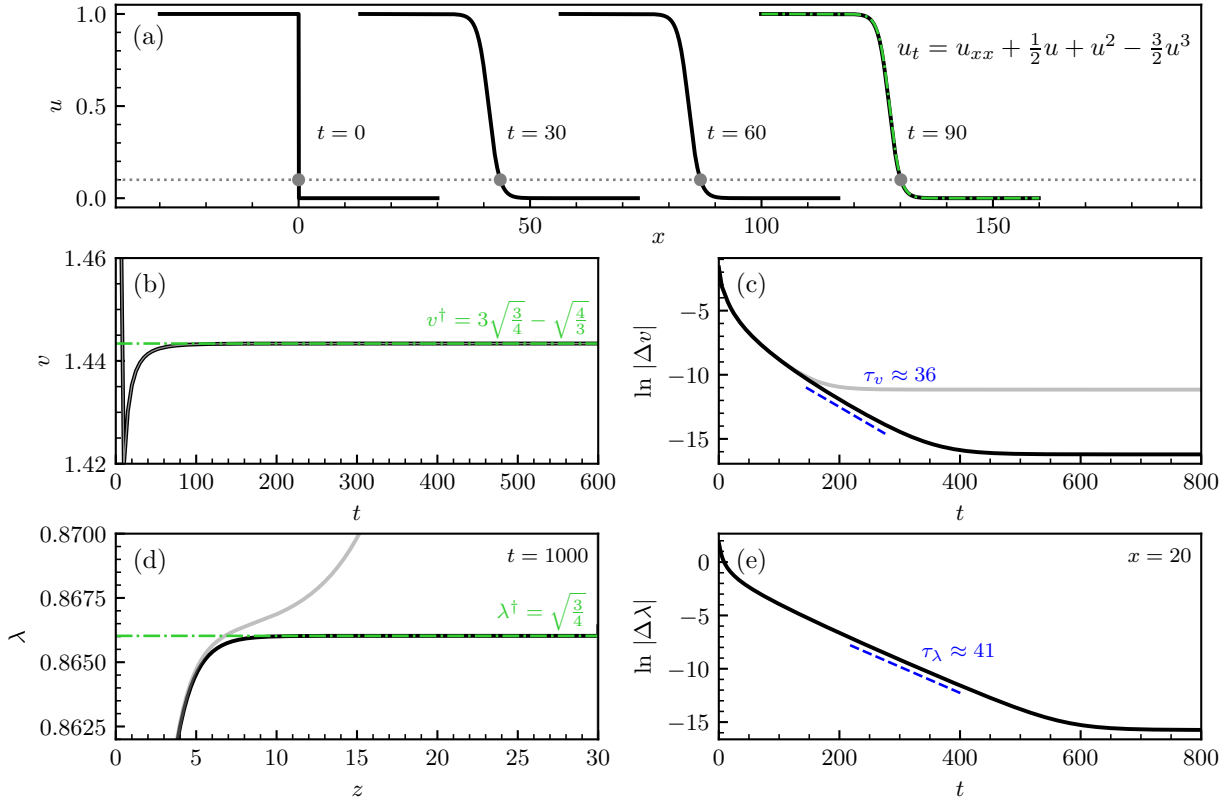


FIG. 9. The GBC method benchmarks well for the pushed front solutions of Eq. (22) with  $a = 1/2$  and a step function initial condition. The simulation parameters are  $dt = 0.025$ ,  $t \in [0, 1000]$ ,  $dx = 0.001$ ,  $x \in [-30, 30]$ , with a moving frame speed  $c = v^\dagger = 3\sqrt{3/4} - \sqrt{4/3}$  and a buffer region of size  $\delta = 10$ . (a) The simulated front (solid, black) propagates through the lab-frame and is visualized at four snapshots from  $t = 0$  to  $t = 90$ . The simulated front agrees with the theoretical front solution (dash-dotted, green) at  $t = 90$ . (b) The front velocity  $v(t)$  in the lab frame compared between the GBC method (solid, black) and DZ method (solid, gray). Both methods approach the theoretically predicted front velocity (dash-dotted, green) and are visually indistinguishable. (c) Comparison of the velocity deviation  $\Delta v = v - v^\dagger$  between the two methods demonstrates a significant improvement in precision with the GBC method. Exponential convergence is in agreement with theoretical predictions [12], and the extracted time constant via log-linear fitting is  $\tau_v \approx 36$ . The fitting region (dashed, blue) is chosen according to [34]. (d) The front steepness  $\lambda = -u_x/u$  computed at  $t = 1000$  in the moving frame coordinate  $z = x - \int_0^t c(t') dt'$  shows an accurate value of leading edge steepness  $\lambda^\dagger = \sqrt{3/4}$  in the GBC method and an inaccurate value for the DZ method. (e) The deviation in front steepness  $\Delta \lambda = \lambda - \lambda^\dagger$  for the GBC method over time, where the front steepness is calculated at  $x = 20$  at each time step. The time constant  $\tau_\lambda \approx 41$  is extracted via log-linear fitting.

## B. Nonautonomous pushed fronts and the pushed-pulled transition

We next modify Eq. (22) to read

$$u_t = u_{xx} + a(t)u + u^2 - (1 + a(t))u^3, \quad (26)$$

starting with a linear time-dependence of the form

$$a(t) = 0.001t \quad (27)$$

for  $t \in [0, 300]$ . Substituting Eq. (27) into Eq. (24), we obtain the time-frozen asymptotic speed as

$$v^\dagger(t) = 3\sqrt{\frac{0.001t + 1}{2}} - \frac{1}{0.001t}. \quad (28)$$

We simulate Eq. (26) using the GBC method, the results of which are shown in Fig. 10. We find that the numerically computed velocity quickly approaches the time-frozen asymptotic pushed speed (28) as the time step  $dt$  is reduced. Since there is exponential convergence to the pushed front in the autonomous case, and we only impose linear growth

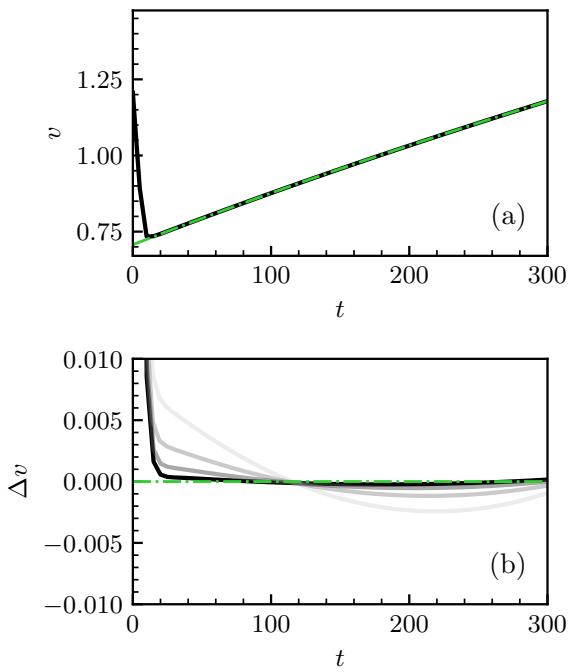


FIG. 10. A linearly increasing time-dependent parameter  $a(t) = 0.001t$  demonstrates convergence to the time-frozen asymptotic front velocity following Eq. (28). The simulation parameters are  $t \in [0, 300]$ ,  $dx = 0.001$ ,  $x \in [-50, 200]$ ,  $\gamma = 0.9$  and  $\delta = 10$  with varying temporal resolutions. The time step size takes on the values  $dt \in \{0.2, 0.1, 0.05, 0.025\}$  with smaller values depicted in progressively darker shades of gray in (b). These gray curves converge to the most accurate simulation at  $dt = 0.025$  (solid, black) indicating that as  $dt \rightarrow 0$ , the simulated front velocity converges to the time-frozen asymptotic velocity (dash-dotted, green).

for  $a(t)$ , this result seems reasonable.

Given the above analysis, pushed front convergence appears straightforward, but below we reveal more subtle behavior by analyzing the dynamic pushed-to-pulled transition. This transition is an ideal phenomenon to study with the GBC method for its inherent time-dependence and long-time pulled behavior.

Recall that in the autonomous case (22), pushed fronts are selected for  $a < 1$  and pulled fronts are selected for  $a > 1$ . At the pushed-pulled transition  $a = 1$ , the pushed and pulled fronts converge. In particular,  $v^\dagger = v^*$ . The pushed-pulled transition is a codimension-one bifurcation [37] and is an example of a global bifurcation: it is associated with a change in the qualitative behavior of a heteroclinic orbit in the phase plane [3].

The dynamic crossing of a bifurcation point can lead to a phenomenon known as *bifurcation delay*

[16, 38], in which the onset of the bifurcation occurs later than the time at which the bifurcation parameter crosses the time-frozen critical value. Delay phenomena in pushed-pulled transitions have recently been observed [19].

Bifurcation delay arises in our problem via pushed-pulled competition. For concreteness, we take  $a(t)$  to be algebraically increasing, e.g.  $a(t) = (\epsilon t)^\alpha$  for  $\epsilon, \alpha > 0$ . Initially, the pushed front velocity is faster than the pulled front velocity, so in the comoving frame of the pushed front, the linear equation is only convectively unstable; that is, linear perturbations are driven away in the comoving frame [3]. However, as  $t$  increases, the linear equation becomes absolutely unstable, and we expect those linear modes to return and take over.

When does the convective instability become an absolute instability in the frame of the pushed front? It is natural to assume that this turnaround will occur when  $a(t) = 1$ , but this is not the case. For algebraically increasing  $a(t)$ , the natural asymptotic velocity  $v^{**}(t)$  is larger than the time-frozen one  $v^*(t)$ . Therefore,  $v^{**}(t)$  attains (and passes)  $v^\dagger(t)$  at an earlier time than when  $a(t) = 1$ , so the turnaround occurs earlier. However, at the turnaround, the linear modes have receded; it is only when they return that we see the result: a pushed-pulled transition.

With this idea in mind, we can define the *turnaround times*  $t^*$  and  $t^{**}$  such that

$$v^\dagger(t^*) = v^*(t^*), \quad (29a)$$

$$v^\dagger(t^{**}) = v^{**}(t^{**}). \quad (29b)$$

Then, we can define the theoretical *pushed-pulled transition time*  $t_{\text{pp}} > 0$  as the time that solves

$$\int_0^{t_{\text{pp}}} [v^{**}(t) - v^\dagger(t)] dt = 0. \quad (30)$$

This articulates the discussion above. For  $t < t_{\text{pp}}$ , the pushed front moves faster. For  $t > t_{\text{pp}}$ , the pulled front moves faster. For algebraic growth, the integral (30) has a closed form; see Appendix C. Finally, we can define delay times

$$t_{\text{delay}}^* = t_{\text{pp}} - t^*, \quad (31a)$$

$$t_{\text{delay}}^{**} = t_{\text{pp}} - t^{**} \quad (31b)$$

We interpret  $t_{\text{delay}}^*$  as bifurcation delay; it is the additional time after the time-frozen bifurcation point before observing the effect of the bifurcation. We interpret  $t_{\text{delay}}^{**}$  as the time it takes for the linear modes to take over after the turnaround. We do not refer to this quantity as bifurcation delay, since it does not refer to a time-frozen bifurcation; rather, it is a separate quantity.

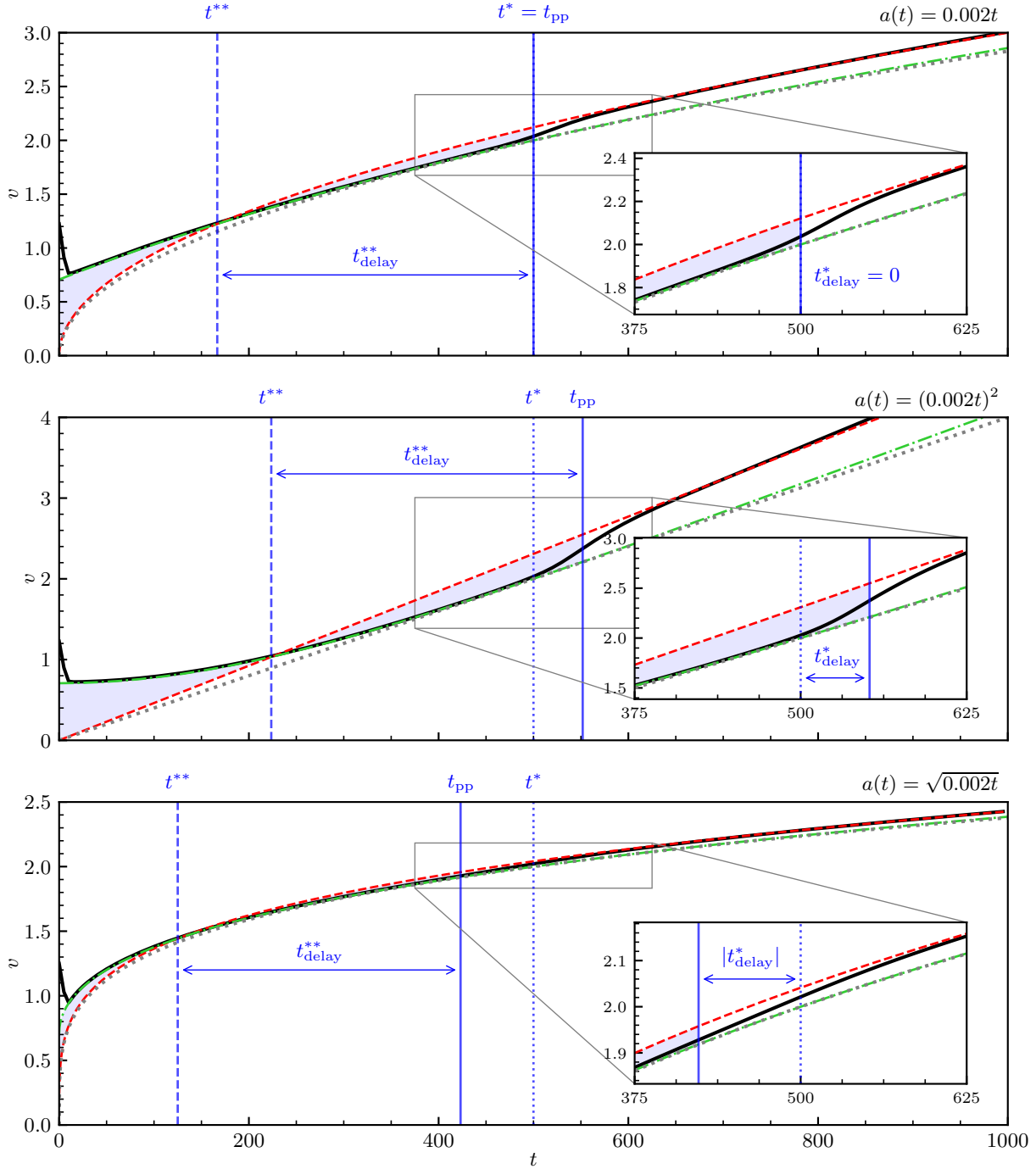


FIG. 11. Simulated pushed-pulled transitions in Eq. (26) starting from a step initial condition for  $a(t) = \epsilon t$  (top),  $a(t) = (\epsilon t)^2$  (middle), and  $a(t) = \sqrt{\epsilon t}$  (bottom) with  $\epsilon = 0.002$  show zero, positive, and negative bifurcation delay, respectively, in agreement with theory. Initially, the measured velocity (solid, black) follows the time-frozen pushed velocity  $v^f(t)$  (dash-dotted, green). Then, the front leaves the pushed regime and approaches the natural pulled asymptotic velocity  $v^*(t)$  (dotted, red). The time-frozen pulled asymptotic velocity  $v^*(t)$  (dotted, gray) is shown for reference. In each case, we observe that the pushed-pulled transition occurs near  $t_{\text{pp}}$  (solid, blue), the theoretical transition point (30) at which the integral of the velocity difference  $v^*(t) - v^f(t)$  (shaded blue region) vanishes. The velocity crossing times  $t^*$  (dotted, blue) (29a) and  $t^{**}$  (dashed, blue) (29b) and their corresponding delays  $t_{\text{delay}}^*$  (31a) and  $t_{\text{delay}}^{**}$  (31b) are also shown.

In Fig. 11, we simulate the dynamic crossing of the pushed–pulled transition for linear, quadratic, and square root growth of  $a(t)$ . The data confirms the idea outlined above: the pushed–pulled transition occurs when Eq. (30) holds. For linear growth, coincidentally  $t_{\text{pp}} = t^*$ , thus  $t_{\text{delay}}^* = 0$  and no bifurcation delay is observed (see Appendix C). This behavior is not generic across other forms of algebraic growth. For quadratic growth, we observe bifurcation delay  $t_{\text{delay}}^* > 0$ . For square root growth, we remarkably find  $t_{\text{delay}}^* < 0$ , i.e. *negative bifurcation delay*. In each case, the ordering of  $t_{\text{pp}}$  and  $t^*$  is independent of the growth rate  $\epsilon$ . Of course, in each case, we also observe  $t_{\text{delay}}^{**} > 0$ .

To compare the simulations with theory more precisely, we define an empirical measure of the transition progress as the relative velocity deviation from  $v^\dagger(t)$ :

$$\frac{v(t) - v^\dagger(t)}{v^{**}(t) - v^\dagger(t)} \times 100\%. \quad (32)$$

In Fig. 12, we measure the 20%, 50%, and 80% completion times. The 20% completion time characterizes the *exit time* when the solution leaves the neighborhood of the original attractor; neighborhood exit is the typical definition of bifurcation onset in the context of bifurcation delay (cf. [16]). In all cases, the measured 20% and 50% completion times in Fig. 12 are qualitatively consistent with the transition time predicted by  $t_{\text{pp}}$ . The 80% completion time characterizes the *entrance time* into the neighborhood of the new attractor, and this time depends on the asymptotic properties of the attractor. Measuring the entrance time implicitly assumes that the front speed converges to the natural asymptotic velocity. This is not true in general (Fig. 5) but is expected for monotonically increasing  $a(t)$  (see Sec. III). Further, we speculate that algebraic growth of  $a(t)$  with a larger power of  $t$  causes faster convergence to  $v^{**}(t)$ . This is consistent with Fig. 12, where the transition duration is indeed seen to shorten with increasing power.

We conclude this section with a few additional remarks. Although our results are consistent, we recognize that it is not clear how to precisely define the onset of the transition. The theoretical value  $t_{\text{pp}}$  as defined by Eq. (30) does not consider transient behavior that would add additional terms depending on the initial condition. Additionally, the empirical measure proposed in Eq. (32), defined via velocities, is likely inadequate. In fact, the height  $H$  at which the front is tracked results in slightly different velocity curves (see Eq. (18)), although for the convergent cases we expect  $H$  dependence to appear only in higher-order terms as is true in the autonomous case [3]. A proper definition should rely on an underly-

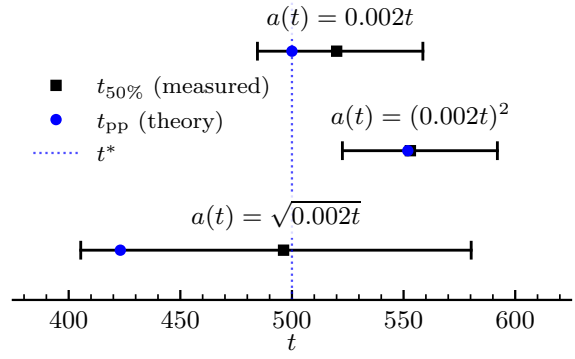


FIG. 12. Timing of the simulated pushed–pulled transitions in Fig. 11 confirms theoretical predictions. For each simulation, we measure the times at which the transition progress (32), defined in terms of the velocity difference from  $v^\dagger(t)$ , is 20% (left endpoint), 50% (middle black square), and 80% (right endpoint). The theoretical transition time  $t_{\text{pp}}$  (solid, blue) and the time-frozen transition time  $t^*$  (dashed, blue) are drawn for reference. In each case, we find that  $t_{\text{pp}}$  accurately describes the transition time. The 20% and 50% completion times are ordered correctly. Notably, for square root growth, the transition is more than halfway complete by  $t^* = 500$ , thus confirming negative bifurcation delay. The transition durations vary, and the 80% point deviates from the predicted ordering, but these facts are not surprising due to the different asymptotic behaviors of each of the pulled regimes.

ing metric to characterize the distance between the asymptotic pushed and pulled fronts. One can then precisely define the neighborhoods to determine the exit time and transition duration [16].

Finally, in the original example of a nonautonomous pushed front (Fig. 10), the simulation time is restricted so that  $v^{**}(t) < v^\dagger(t)$  and thus  $t < t^{**}$  for all  $t$ . Therefore, the simulation remains within the pushed regime. However, in light of these results, it is important to consider that, in general, pulled front competition must be considered even in cases that appear entirely pushed if analyzed adiabatically.

## V. DISCUSSION

The GBC method enables accurate simulation of front propagation in the F-KPP equation by enforcing a time-dependent boundary condition at the leading edge, enabling precise measurements of front velocities even on relatively small computational domains. The GBC benchmarks well against known results for the autonomous Fisher equation with both steep and shallow initial conditions. This contrasts

with previous approaches, which typically require different boundary conditions for steep and shallow initial data. Furthermore, the GBC method can handle time-dependent growth and diffusion coefficients, revealing complex nonlinear dynamics that deviate from the predictions of linear theory for pulled fronts. The same numerical framework is also capable of precisely simulating pushed fronts and the pushed–pulled transition, revealing both delayed and premature transition onset dictated by the competition between the two regimes.

Much remains to be understood about the nature of fronts with a time-dependent parameter. How the natural asymptotic velocity and profile characterize pulled fronts beyond the simplest cases remains poorly understood. A more careful approach is needed to understand the asymptotics of pulled fronts beyond the simple linear analysis presented here. The influence of time-dependent parameters on shallow initial conditions is also largely unexplored. The transition from a “shallow” to “steep” regime and vice versa is not a phenomenon that can occur in the autonomous problem. For pushed fronts, the pushed–pulled transition offers a particularly rich setting for exploring global bifurcation delay in a spatially extended system. The delayed and premature onset of the transition joins the set of novel phenomena induced by a time-dependent forcing along with other nonautonomous behaviors such as rate-induced tipping [39]. Understanding the geometry and topology of the pushed–pulled transition would be valuable for improving the robustness of the current results. We now have a powerful numerical tool to explore these questions and more.

A rigorous numerical analysis of the GBC method, beyond the proof-of-concept validation presented here, remains an important direction for future work. Perhaps most importantly, we need a better understanding of the accuracy and stability of this method. We also have a limited understanding of how to select the buffer size  $\delta$  for general time-dependent parameters. We also restrict ourselves here to a Dirichlet-to-Dirichlet boundary condition, where the NL region provides a Dirichlet condition for the LA region, which in turn provides a Dirich-

let condition for the NL region. One could consider other combinations, e.g. Dirichlet-to-Neumann or Neumann-to-Dirichlet, which may have different stability and accuracy properties. Finally, we have not considered the derivable corrections to the front velocity due to discretization [3, 24, 25].

The foundational finite-difference scheme can also be improved. Here, we used a simple first-order IMEX Euler scheme in time with second-order central finite differences in space. Parabolic equations such as F-KPP are often simulated with Crank-Nicolson, other IMEX/implicit schemes, or other specialized schemes [24, 32, 40]. To resolve the time-dependent parameters more accurately, one may consider a smaller time step. However, this would require optimizations or approximations to the GBC method to avoid excessive numerical integration time to compute the boundary value (see Appendix B).

Finally, we can consider more complex equations. The GBC method can currently only be applied to the one-dimensional nonautonomous F-KPP equation with a somewhat restrictive requirement on the moving frame speed. These restrictions arise from the need to construct a half-line Green’s function and evaluate the linear solution in closed form via Gaussian integrals. Developing analytical and/or numerical tools to relax these restrictions—by approximating the relevant integrals, for instance—would enable the GBC method to be applied to a wider variety of problems, including those with higher-order spatial derivatives or even spatial heterogeneities [41, 42].

## ACKNOWLEDGMENTS

We gratefully acknowledge helpful comments and suggestions from C. Liu and V. Klika. This work was supported by the Berkeley Physics-and-Astronomy Undergraduate Research Scholars (BPURS) Program (T.T. and S.M.), a US Dynamics Days travel stipend (S.M.) and by the National Science Foundation under grant DMS-2308337 (T.T. and E.K.).

---

[1] R. A. Fisher, *Annals of Eugenics* **7**, 355 (1937).

[2] A. Kolmogorov, I. Petrovsky, and N. Piskunov, in *Dynamics of Curved Fronts* (Elsevier, 1988) pp. 105–130.

[3] W. van Saarloos, *Phys. Rep.* **386**, 29 (2003).

[4] H. Berestycki and G. Nadin, *Asymptotic spreading for general heterogeneous Fisher-KPP type equations*, Mem. Am. Math. Soc., Vol. 280 (American Mathematical Society, 2022).

[5] M. Avery, M. Holzer, and A. Scheel, [arXiv:2508.14864](https://arxiv.org/abs/2508.14864) (2025).

[6] M. Avery, M. Holzer, and A. Scheel, [arXiv:2512.07764](https://arxiv.org/abs/2512.07764) (2025).

[7] D. G. Aronson and H. F. Weinberger, in *Partial Differential Equations and Related Topics*, Vol. 446, edited by J. A. Goldstein (Springer Berlin Heidelberg, 2008).

berg, Berlin, Heidelberg, 1975) pp. 5–49, series Title: Lecture Notes in Mathematics.

- [8] D. G. Aronson and H. F. Weinberger, *Adv. Math.* **30**, 33 (1978).
- [9] M. Bramson, *Convergence of solutions of the Kolmogorov equation to travelling waves*, Mem. Am. Math. Soc., Vol. 44 (American Mathematical Society, 1983).
- [10] M. Avery and A. Scheel, *Commun. Amer. Math. Soc.* **2**, 172 (2022).
- [11] V. Klika, E. A. Gaffney, and P. K. Maini, *Physica D* **467**, 134268 (2024).
- [12] F. Rothe, *Rocky Mountain J. Math.* **11**, 617 (1981).
- [13] W. van Saarloos, *Phys. Rev. A* **39**, 6367 (1989).
- [14] E. Knobloch and R. Krichetnikov, *Acta Appl. Math.* **137**, 123 (2014).
- [15] R. Goh and A. Scheel, *Nonlinearity* **36**, R1 (2023).
- [16] T. Tsubota, C. Liu, B. Foster, and E. Knobloch, *Phys. Rev. E* **109**, 044210 (2024).
- [17] A. Ducrot and Z. Jin, *Nonlinear Anal.: Real World Appl.* **74**, 103923 (2023).
- [18] L. Alzaleq and V. Manoranjan, *IOP SciNotes* **1**, 025003 (2020).
- [19] M. Avery, O. Garcia-Lopez, R. Goh, B. Hosek, and E. Shade, *Physica D* **483**, 134972 (2025).
- [20] V. Mendez, J. Fort, and T. Pujol, *J. Phys. A: Math. Gen.* **36**, 3983 (2003).
- [21] G. Nadin and L. Rossi, *J. Math. Pures Appl.* **98**, 633 (2012).
- [22] E. Brunet and B. Derrida, *Phys. Rev. E* **56**, 2597 (1997).
- [23] D. Panja and W. van Saarloos, *Phys. Rev. E* **65**, 057202 (2002).
- [24] U. Ebert and W. van Saarloos, *Physica D* **146**, 1 (2000).
- [25] B. C. Ponedel, H.-C. Kao, and E. Knobloch, *Phys. Rev. E* **96**, 032208 (2017).
- [26] S. Zhao and G. W. Wei, *SIAM J. Sci. Comput.* **25**, 127 (2003).
- [27] D. Givoli, *Arch. Comput. Methods Eng.* **6**, 71 (1999).
- [28] D. Givoli, *Numerical Methods for Problems in Infi-* *nite Domains*, Studies in Applied Mechanics, Vol. 33 (Elsevier, 2013).
- [29] J. B. Keller and D. Givoli, *J. Comp. Phys.* **82**, 172 (1989).
- [30] D. Givoli, in *Computational Acoustics of Noise Propagation in Fluids – Finite and Boundary Element Methods*, edited by S. Marburg and B. Nolte (Springer, Berlin, 2008) pp. 145–166.
- [31] A. Ditkowskii and A. Suhov, *Proc. Natl. Acad. Sci. U.S.A.* **105**, 10646 (2008).
- [32] T. Hagstrom and H. B. Keller, *SIAM J. Sci. Stat. Comput.* **7**, 978 (1986).
- [33] H. S. Carslaw and J. C. Jaeger, *Conduction of Heat in Solids*, 2nd ed. (Oxford University Press, Oxford, 1959).
- [34] V. Deshmukh, E. Bradley, J. Garland, and J. D. Meiss, *Chaos* **31**, 123102 (2021).
- [35] J. Nagumo, S. Arimoto, and S. Yoshizawa, *Proc. IRE* **50**, 2061 (1962).
- [36] H. McKean Jr., *Adv. Math.* **4**, 209 (1970).
- [37] M. Avery, M. Holzer, and A. Scheel, *J. Nonlinear Sci.* **33**, 102 (2023).
- [38] E. Benoît, ed., *Dynamic Bifurcations*, Lecture Notes in Mathematics No. 1493 (Springer-Verlag, Berlin, 1991).
- [39] S. Wieczorek, C. Xie, and P. Ashwin, *Nonlinearity* **36**, 3238 (2023).
- [40] R. E. Mickens, *Numer. Meth. Partial Differ. Equ.* **10**, 581 (1994).
- [41] R. Kuske and W. Eckhaus, *SIAM J. Appl. Math.* **57**, 112 (1997).
- [42] R. Goh, T. J. Kaper, A. Scheel, and T. Vo, *SIAM J. Appl. Dyn. Sys.* **22**, 2312 (2023).
- [43] S. Redner, *A Guide to First-Passage Processes* (Cambridge University Press, 2001).
- [44] L. C. Evans, *Partial Differential Equations*, 2nd ed., Graduate Studies in Mathematics (Amer. Math. Soc., Providence, R.I., 2010).
- [45] R. L. Burden and J. D. Faires, *Numerical Analysis*, 9th ed. (Brooks/Cole, Cengage Learning, 2011).

## Appendix A: Theoretical Details

We seek an exact solution of the linearized, nonautonomous F-KPP equation on the half-line  $x \in [0, \infty)$  with an arbitrary initial condition and an arbitrary time-dependent Dirichlet boundary value:

$$u_t = a(t)u + c(t)u_x + d(t)u_{xx}, \quad (\text{A1a})$$

$$u(x, 0) = f(x), \quad (\text{A1b})$$

$$u(0, t) = g(t). \quad (\text{A1c})$$

We begin by finding the free Green's function, i.e. the Green's function for the infinite line. By taking the Fourier transform of (A1a) in  $x$ , we obtain the (time-dependent) dispersion relation

$$\omega(k, t) = -kc(t) + i[a(t) - k^2d(t)]. \quad (\text{A2})$$

The resulting free Green's function for delta forcing at  $(y, s)$  is

$$G_{\text{free}}(x, t; y, s) = \frac{1}{\sqrt{4\pi\tilde{D}(t, s)}} \exp \left[ \tilde{A}(t, s) - \frac{(x - y + \tilde{C}(t, s))^2}{4\tilde{D}(t, s)} \right], \quad (\text{A3})$$

where  $\tilde{A}(t, s) = A(t) - A(s)$ , with  $A(t) = \int_0^t a(t')dt'$  as in Eq. (15), and  $\tilde{C}(t, s)$  and  $\tilde{D}(t, s)$  defined similarly.

We can now use the free Green's function to construct the half-line Green's function. In the case  $g(t) = 0$ , we use the method of images. Naïvely, we may expect to use a symmetric image charge, but advection due to the moving frame breaks the reflection symmetry. To resolve this matter, we take inspiration from [43], seeking a weighted image charge that satisfies the desired boundary condition  $u(0, t) = 0$ :

$$0 = G_{\text{free}}(0, t; y, s) - \alpha G_{\text{free}}(0, t; -y, s). \quad (\text{A4})$$

We solve Eq. (A4) to find that

$$\alpha = e^{\frac{c(t)}{d(t)}y}. \quad (\text{A5})$$

In order for Eq. (A4) to solve Eq. (A1), the weight  $\alpha$  must be time-independent. Hence, to proceed further, we require that  $c(t)$  be proportional to  $d(t)$ . We define the proportionality constant  $\gamma$  so that  $c(t) = \gamma d(t)$  and  $\alpha = e^{\gamma y}$ . The half-line Green's function is

$$G(x, t; y, s) = G_{\text{free}}(x, t; y, s) - e^{\gamma y} G_{\text{free}}(x, t; -y, s) \quad (\text{A6})$$

and the solution to the original problem, with  $g(t) = 0$ , is then

$$u(x, t) = \int_0^\infty G(x, t; y, 0) f(y) dy. \quad (\text{A7})$$

For the case  $g(t) \neq 0$ , we may naïvely proceed with the change-of-variable  $v(x, t) = u(x, t) - g(t)$ . This substitution converts the boundary condition into an inhomogeneous forcing  $F(t) = -g'(t)$ . However, because this forcing is constant for all  $x$  and  $\lim_{t \rightarrow \infty} \int_0^\infty G(x, t; y, s) dy$  is not finite, the resulting solution is not well-behaved as  $t \rightarrow \infty$ . Therefore, we pick a different substitution that enforces regularity. The inhomogeneous forcing must decay as  $x \rightarrow \infty$ , so we consider the substitution

$$w(x, t) = u(x, t) - g(t) e^{-x^2}. \quad (\text{A8})$$

Note that an exponential decay term  $g(t)e^{-rx}$  would require tuning the decay rate  $r$  to be large enough to ensure a finite limit; the Gaussian term is thus a preferable substitution. The resulting equation is

$$w_t = a(t)w + c(t)w_x + d(t)w_{xx} + F(x, t) \quad (\text{A9a})$$

$$w(x, 0) = f(x) - g(0) e^{-x^2} \quad (\text{A9b})$$

$$w(0, t) = 0 \quad (\text{A9c})$$

$$F(x, t) = [(a(t) - 2d(t))g(t) - g'(t)]e^{-x^2} - 2c(t)g(t)xe^{-x^2} + 4d(t)g(t)x^2e^{-x^2}. \quad (\text{A9d})$$

By appealing to Duhamel's principle [44], we can write down the exact solution to Eq. (A1) as

$$u(x, t) = g(t) e^{-x^2} + \int_0^\infty G(x, t; y, 0) [f(y) - g(0) e^{-y^2}] dy + \int_0^t \int_0^\infty G(x, t; y, s) F(y, s) dy ds. \quad (\text{A10})$$

The final term may be written as

$$\int_0^t \int_0^\infty G(x, t; y, s) F(y, s) dy ds = \int_0^t [h_0(s)I_0(x, t; s) + h_1(s)I_1(x, t; s) + h_2(s)I_2(x, t; s)] ds, \quad (\text{A11})$$

where

$$h_0(t) = [a(t) - 2d(t)]g(t) - g'(t), \quad I_0(x, t; s) = \int_0^\infty G(x, t; y, s)e^{-y^2} dy, \quad (\text{A12a})$$

$$h_1(t) = -2c(t)g(t), \quad I_1(x, t; s) = \int_0^\infty G(x, t; y, s)ye^{-y^2} dy, \quad (\text{A12b})$$

$$h_2(t) = 4d(t)g(t), \quad I_2(x, t; s) = \int_0^\infty G(x, t; y, s)y^2e^{-y^2} dy. \quad (\text{A12c})$$

Since  $G(x, t; y, s)$  is of Gaussian form, the integrals  $I_k$  have closed-form expressions which all converge to a finite limit as  $t \rightarrow \infty$ .

## Appendix B: Numerical Details

### 1. Detailed algorithm

The numerical algorithm for the GBC method is built upon a standard finite-difference method. Formally, let  $N_x$  and  $N_t$  be the number of spatial grid points and time steps, respectively. For the field  $u(x, t)$ , define the discrete numerical approximation as  $\tilde{u}(x_j, t^{(i)}) = \tilde{u}_j^{(i)}$  where  $t^{(i)} = i dt$  for  $i = 0, \dots, N_t - 1$  and  $x_j = x_0 + j dx$  for  $j = 0, \dots, N_x$ . Additionally, define  $a(t^{(i)}) = a^{(i)}$ ,  $c(t^{(i)}) = c^{(i)}$ , and  $d(t^{(i)}) = d^{(i)}$ .

The finite difference equation at time  $t^{(i)}$  for  $j = 1, \dots, N_x - 1$ , with second-order central differences in space and an implicit-explicit (IMEX) Euler scheme in time is

$$\frac{\tilde{u}_j^{(i+1)} - \tilde{u}_j^{(i)}}{dt} = a^{(i+1)}\tilde{u}_j^{(i+1)} + c^{(i+1)} \left[ \frac{\tilde{u}_{j+1}^{(i+1)} - \tilde{u}_{j-1}^{(i+1)}}{2 dx} \right] + d^{(i+1)} \left[ \frac{-\tilde{u}_{j+1}^{(i+1)} + 2\tilde{u}_j^{(i+1)} - \tilde{u}_{j-1}^{(i+1)}}{(dx)^2} \right] + \mathcal{N}(\tilde{u}_j^{(i)}, t^{(i)}) \quad (\text{B1a})$$

where  $\mathcal{N}(u, t)$  are the nonlinear terms in  $f(u, t)$ , which are treated explicitly. For the boundary terms, we have

$$\tilde{u}_0^{(i+1)} = \tilde{u}_1^{(i+1)} \quad (\text{B1b})$$

$$\tilde{u}_{N_x}^{(i+1)} = \tilde{b}^{(i+1)}. \quad (\text{B1c})$$

Here,  $\tilde{b}^{(i)} = \tilde{b}(t^{(i)})$  is the GBC Dirichlet boundary value. This completes a system of  $N_x + 1$  linear equations, which can be solved to determine  $\tilde{u}^{(i+1)}$ .

As depicted in Fig. 2, we compute  $\tilde{b}^{(i+1)}$  prior to the implicit step. To do so, we build an array of  $\tilde{g}^{(i)} = \tilde{u}(x_1 - \delta, t^{(i)})$  and its time derivative  $\tilde{g}'^{(i)}$ . At time  $t^{(i)}$ , we perform the following steps:

1. Measure the current value  $\tilde{g}^{(i)}$ .
2. Compute  $\tilde{g}'^{(i)}$  as a first-order right-handed derivative.
3. Compute the integral (A11) using the trapezoidal rule with step size  $dt$ .
4. Compute the final result (A10). This is  $\tilde{b}^{(i+1)}$ .

Because the integrals  $I_k$  are independent of the simulation, we can precompute the  $N_t^2$  values for each  $I_k$ . We can also precompute the  $N_t$  values for the initial condition integral (the second term in Eq. (A10)). Thus, the dominant compute time contribution in computing  $\tilde{b}^{(i+1)}$  is Eq. (A11), which takes  $\mathcal{O}(N_t)$  time. Solving Eq. (B1) using a sparse solver takes  $\mathcal{O}(N_x)$ . Altogether, the whole algorithm takes  $\mathcal{O}(N_t^2 + N_t N_x)$  time.

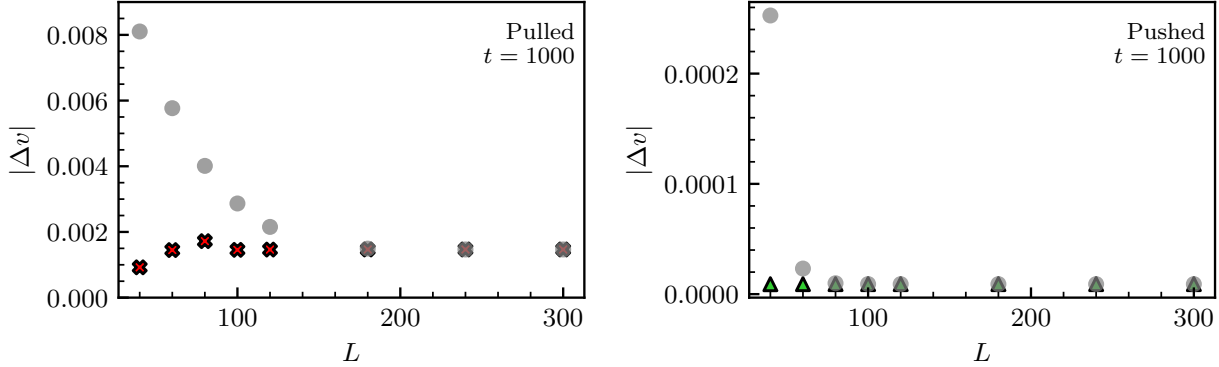


FIG. 13. For the autonomous F-KPP equation (see Figs. 3 and 9) in large computational domain sizes  $L = x_1 - x_0$ , the GBC method measures the same long-time front velocity as the DZ method (gray dots) in both the pulled (red X's) and pushed (green triangles) regimes. For small domain sizes  $L$ , the GBC method outperforms the DZ method, with larger improvements for pulled fronts as expected. Here,  $\Delta v$  is the deviation from the relevant asymptotic velocity at the finite time  $t = 1000$ , so this does not necessarily capture error from ground truth. Simulation parameters are  $dt = 0.025$ ,  $dx = 0.01$ , and  $\delta = 10$ .

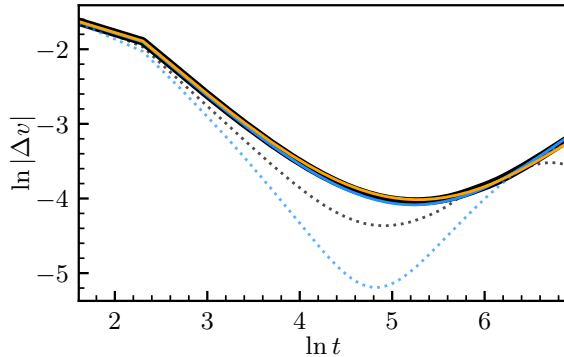


FIG. 14. The choice of  $\gamma = c(t)/d(t)$  affects the numerically measured velocity deviation  $\Delta v$ . For the nonautonomous pulled front with  $d(t) = 1 + \epsilon t$ ,  $\epsilon = 0.001$ , the original choice of  $\gamma = 1.65$  (black), is reproduced from Fig. 5(c), while alternative choices  $\gamma = 1.55$  (blue) and  $\gamma = 1.75$  (orange) are overlaid. A comparison of the curves for  $dt = 0.025$  (solid) with  $dt = 0.2$  (dotted) shows that a different choice of  $\gamma$  becomes less important as  $dt$  is reduced.

## 2. Convergence

In the main text, we have provided numerical evidence indicating that the method converges as  $dt \rightarrow 0$ . In particular, in Figs. 3, 4, and 9, we demonstrate good agreement with existing theoretical predictions of the front speed in the autonomous case. We also have agreement, in Fig. 7, with recent results on convergence for linear growth in the growth parameter [19].

In Fig. 13, we show furthermore that the GBC method converges to the DZ method as the domain size  $L \rightarrow \infty$  as expected. The convergence in the pushed regime is much faster than in the pulled regime, as expected generically for numerical methods for fronts [6]. Importantly, the GBC method faithfully returns the correct front speed even with relatively small  $L$ , thus eliminating the need for a large domain size.

Our last convergence result concerns the frame speed, i.e. the choice of  $\gamma = c(t)/d(t)$ . Ideally, one would select  $\gamma$  so that the front is near-stationary in the moving frame. Roughly speaking, if the solution varies slowly relative to the time step, the error is smaller. More precisely, the error for Euler's method (explicit and implicit) applied to a one-dimensional ordinary differential equation is bounded by  $dt \cdot \max |y''(t)|$ , where  $y''(t)$  is the second derivative of the solution [45]. Therefore, for the constant parameter case, we select the

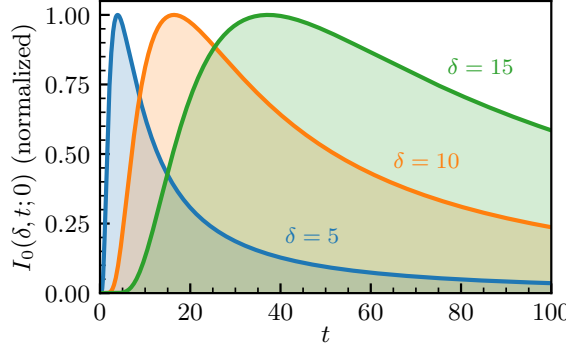


FIG. 15. Effect of buffer size  $\delta$  on the normalized integration kernel  $I_0(x = \delta, t; s = 0)$  (A12a) under the constant Fisher regime  $a(t) = d(t) = 1$  and  $c(t) = \gamma = 2$ . Three buffer sizes  $\delta = 5, 10$ , and  $15$  are shown in blue, orange, and green, respectively, indicating that a smaller buffer size results in a narrower, sharper integration kernel.

asymptotic speed for  $\gamma$ . However, for a nonautonomous regime, there is no natural choice of  $\gamma$  because the front shifts relative to the moving frame; this may induce a larger error. In Fig. 14, we do find differences between  $\gamma = 1.55, 1.65$ , and  $1.75$  for the nonautonomous pulled fronts we simulated in Fig. 5. However, as expected, as  $dt \rightarrow 0$ , the choice of  $\gamma$  becomes unimportant for the main conclusions.

### 3. Buffer size selection

Figure 15 shows the kernel  $I_0(x = \delta, t; s = 0)$  for  $\delta = 5, 10$  and  $15$  in the constant Fisher regime described in Fig. 3, i.e.,  $a(t) = d(t) = 1$  and  $c(t) = \gamma = 2$ . We see that a small buffer region results in a narrow, sharp integration kernel, while a large buffer region results in a wide, flat kernel. Thus, in general, for a fixed  $dt$ , a large buffer region minimizes the numerical integration error. However, an excessively large buffer region would only add unnecessary computation time due to the larger domain.

Additionally, upon examining Fig. 15, it is natural to consider a cutoff for the integral (A11) by setting  $G = 0$  for  $t - s > \Delta$ . This would reduce the numerical integration time from  $\mathcal{O}(N_t)$  to  $\mathcal{O}(1)$  and reduce the initial overhead of precomputing each  $I_k$  from  $\mathcal{O}(N_t^2)$  to  $\mathcal{O}(N_t)$ . This cutoff window  $\Delta$  would be smaller for smaller choices of  $\delta$ . Because we sought exact expressions (Appendix A) in our study, this is not a direction we pursue here but is a worthwhile optimization to consider.

### Appendix C: Pushed–Pulled Transition Time

We compute the theoretical pushed–pulled transition time  $t_{\text{pp}}$  (30) for the quadratic-cubic nonautonomous F-KPP equation (22) with the algebraic growth rate  $a(t) = (\epsilon t)^\alpha$  with  $\epsilon, \alpha > 0$  and a constant diffusion coefficient  $d(t) = 1$ . We can write down the natural asymptotic velocity (15), relevant for pulled fronts, and pushed asymptotic velocity (24) as

$$v^{**}(t) = \frac{\frac{\epsilon^\alpha}{\alpha+1}t^{\alpha+1} + \epsilon^\alpha t^\alpha}{\sqrt{\frac{\epsilon^\alpha}{\alpha+1}t^{\alpha+2}}}, \quad (\text{C1})$$

$$v^\dagger(t) = 3\sqrt{\frac{(\epsilon t)^\alpha + 1}{2}} - \sqrt{\frac{2}{(\epsilon t)^\alpha + 1}}. \quad (\text{C2})$$

Integrating, we find the natural asymptotic position

$$x^{**}(t) = \int_0^t v^{**}(s) ds = 2\sqrt{\frac{\epsilon^\alpha}{\alpha+1}t^{\alpha+2}} \quad (\text{C3})$$

and the pushed asymptotic position

$$x^\dagger(t) = \int_0^t v^\dagger(s) ds = \frac{t}{\sqrt{2}} \left[ {}_2F_1 \left( -\frac{1}{2}, \frac{1}{\alpha}, 1 + \frac{1}{\alpha}, -(\epsilon t)^\alpha \right) - 2\sqrt{\frac{(\epsilon t)^\alpha + 1}{2}} {}_2F_1 \left( 1, \frac{1}{2} + \frac{1}{\alpha}, 1 + \frac{1}{\alpha}, -(\epsilon t)^\alpha \right) \right], \quad (\text{C4})$$

where  ${}_2F_1(a, b, c; z)$  is the hypergeometric function. To find  $t_{\text{pp}}$  in general, one then solves  $x^{**}(t) - x^\dagger(t) = 0$  numerically. However, when  $\alpha = 1$ , this expression simplifies to

$$x^{**}(t) - x^\dagger(t) = 2\sqrt{\frac{\epsilon}{2}t^3} - \sqrt{2} \left[ \frac{1}{\epsilon} \left( 1 + 2\sqrt{\frac{1}{1+\epsilon t}} \right) (-1 + \sqrt{1+\epsilon t}) + t \left( -2\sqrt{\frac{1}{1+\epsilon t}} + \sqrt{1+\epsilon t} \right) \right] = 0. \quad (\text{C5})$$

Then  $t_{\text{pp}} = 1/\epsilon$  solves Eq. (C5), which is the same as the time-frozen transition time  $t^*$ , i.e.,  $a(t_{\text{pp}}) = 1$ . Figures 11 and 12 compare these results with simulations.